

Exotic laser beam engineering with coherent fiber-array systems

Svetlana L Lachinova¹ and Mikhail A Vorontsov^{1,2}

¹ Optonicus, 711 East Monument Avenue, Suite 101, Dayton, OH 45402, USA

² Intelligent Optics Laboratory, School of Engineering, University of Dayton, 300 College Park, Dayton, OH 45469, USA

E-mail: mvorontsov1@udayton.edu

Received 24 May 2013, accepted for publication 7 August 2013

Published 3 September 2013

Online at stacks.iop.org/JOpt/15/105501

Abstract

A new approach for engineering a variety of unconventional laser beams with complex spatio-temporal characteristics using coherent (coherently combinable) fiber-array laser transmitter systems is proposed and analyzed through numerical simulations. These laser beams, referred to here as exotic beams, include beams with periodic, quasi-periodic, and stochastic spatio-temporal phase modulation. We show that exotic laser beams can be generated in fiber arrays using feedback control systems of different architectures based on a network of beam-tail interference sensors and fiber-integrated phase shifters. Due to the extremely short (nanosecond time scale) response time of these phase shifting elements, the proposed technique permits generation of laser beams with controllable spatial coherence which can be used for mitigation of speckle effects in various applications including directed energy, laser communications, active imaging, and wavefront sensing. Results of analyses and computer simulations of exotic beams are presented for the fiber-array system with seven subapertures.

Keywords: nonlinear dynamics, instabilities and chaos, fiber laser arrays, beam combining, active or adaptive optics, active imaging

(Some figures may appear in colour only in the online journal)

1. Introduction

Fiber-integrated (LiNbO₃-based) elements of recently emerged coherent fiber-array-based laser systems [1, 2] offer unprecedented opportunities for extremely fast (several GHz-rate) control of intensity, phase, and polarization of the outgoing beams at each fiber-array subaperture (beamlets). With a large number of fiber collimators (subapertures), these capabilities provide unique potentials for engineering of laser beams with complex spatio-temporal dynamics (including stochastic) of intensity, phase, and polarization. These combined, i.e., composed of an array of beamlets, laser beams are referred to here as exotic laser beams. We show that a variety of exotic laser beams can be generated in the coherent fiber-array systems by utilizing ideas of local and nonlocal spatial interactions in nonlinear optical feedback systems that were extensively studied in the late 1980s and

1990s [3–8]. Since that time, various unconventional (exotic) laser beams in the form of rotating multi-petal structures, arrays of spatial solitons, and chaotic beams have been experimentally demonstrated using nonlinear 2D-feedback systems based on optically and electronically addressed liquid crystal (LC) phase modulators and nonlinear resonators and interferometers [9–16]. Potential applications of these beams for active imaging, atmospheric turbulence, thermal blooming, and speckle effects mitigation have been widely discussed but their implementation was precluded due to a relatively slow time response of LC phase modulators [6, 17, 18]. The slow response time is not an issue for exotic laser beams that can be generated in the coherent fiber-array laser transmitter systems. For these laser beams, the refractive index inhomogeneities induced by the atmosphere can be considered ‘frozen’ over thousands of exotic beam phase pattern updates. This suggests that on the time scale of

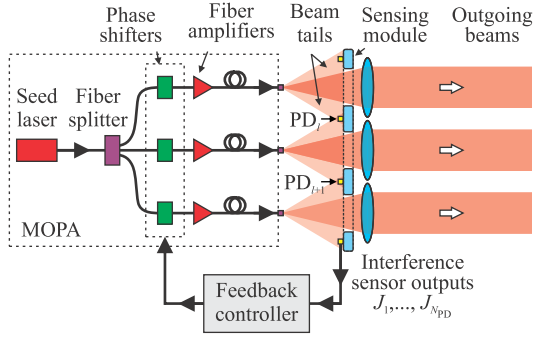


Figure 1. Notional schematic of a coherent fiber array with optoelectronic feedback control system based on beam-tail interference sensors and fiber-integrated phase shifters.

atmospheric turbulence change ($\sim 10^{-3}$ s) these laser beams can be treated as partially coherent optical waves with unusual spatial coherence properties. Partially coherent beams and their propagation properties in turbulent atmosphere has been a topic of extensive theoretical studies [19–24]. The approach proposed here offers an opportunity for practical implementation of these beams.

2. Exotic beam engineering with fiber-array systems

The general idea of exotic laser beam generation is illustrated in figure 1. Assume a coherent fiber-array laser transmitter composed of a narrow-linewidth laser source and a multi-channel master-oscillator power amplifier (MOPA) fiber system based on single-mode polarization-maintaining fiber elements (fiber splitters, phase shifters, and fiber amplifiers). The MOPA system generates an array of N_{sub} Gaussian beams that exit fiber tips located in the fiber-array collimating lens foci [25]. The fiber array in figure 1 includes a sensing module comprised of an array of N_{PD} small (point-size) photo-detectors (PDs) that are assembled at a flat electronic board with holes for the beamlets. The sensing module is located between the collimating lens focal and the pupil planes. The PDs of the sensing module are placed outside the beam cones formed by the fiber tips and collimating lens apertures, as shown in figure 1. As a result, the PDs are illuminated by tail sections of the Gaussian beams that are emitted from the neighboring fiber tips. Overlapping of the beam tails results in their interference. Examples of sensing modules with two different geometries of PDs are illustrated in figure 2 for the fiber-array system with seven subapertures. Note that the seven-subaperture fiber arrays have been implemented experimentally [26]. In the sensing geometry in figures 2(a) and (b), the interference pattern at each PD is formed by tail sections of two beamlets neighboring the PD, while the interference patterns at the PDs in figures 2(c) and (d) result from the interference of three beamlet tails neighboring the PDs. These two sensor types are referred to here as two- and three-tail interference sensors. Both sensing configurations can be implemented in practice. The two-tail sensing architecture is more tolerant to PDs' small displacements from their predefined locations,

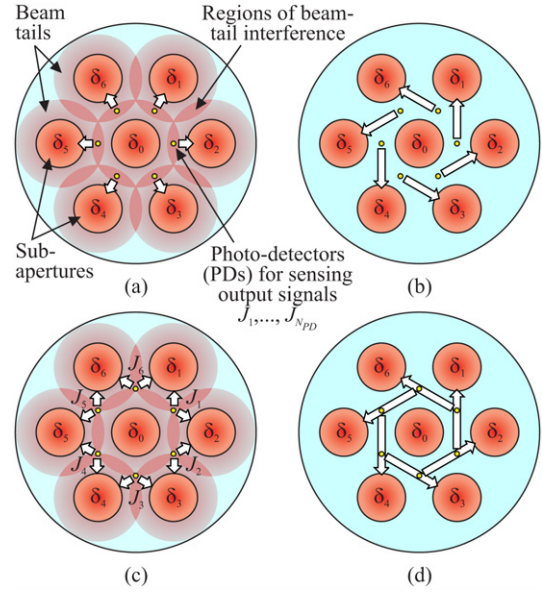


Figure 2. Sensing and control system configurations based on two-tail ((a), (b)) and three-tail ((c), (d)) interference sensors for fiber-array systems with seven subapertures. The transmitter beam subapertures are indicated by solid circles. The beam tails are shown in (a), (c) by semi-transparent areas surrounding the subapertures, and photo-detectors are depicted as small dots inside the overlapping beam tails. The arrows illustrate connectivity between the sensor outputs and control signals applied to the phase shifters in systems with local ((a), (c)) and nonlocal ((b), (d)) spatial interactions. In practice, this connectivity can be easily implemented using an electrical wire connecting the corresponding sensor's output with an amplifier with controllable gain. In its turn, the amplifier output is directly connected with the corresponding phase shifter of the fiber array.

while the three-tail sensing architecture requires fewer sensors [27, 28]. The signals $\{J_1(t), \dots, J_{N_{\text{PD}}}(t)\}$ measured by the PDs are proportional to the interference pattern intensities at PDs' locations at time t .

We ignore the impact on sensor's signals of the beamlet tails corresponding to non-neighboring subapertures. The signal $J_l(t)$ measured by the l th PD, $l = 1, \dots, N_{\text{PD}}$, depends on the piston phases of the closest to this PD's subapertures and is given by [27]

$$J_l(t) = \kappa \{1 + \gamma \cos [\delta_{l'}(t) - \delta_{l''}(t) + \phi_l]\} \quad (1)$$

for two-tail sensing modules in figures 2(a) and (b) and

$$J_l(t) = \kappa \left\{ \frac{3}{2} + \gamma \cos [\delta_{l'}(t) - \delta_{l''}(t) + \phi_l'] + \gamma \cos [\delta_{l''}(t) - \delta_{l'''}(t) + \phi_l''] + \gamma \cos [\delta_{l'''}(t) - \delta_{l'''}(t) + \phi_l'''] \right\} \quad (2)$$

for three-tail sensing arrangements in figures 2(c) and (d). Here $\delta_{l'}(t)$, $\delta_{l''}(t)$, and $\delta_{l'''}(t)$ are the piston phases of the subapertures neighboring the l th photo-detector, and κ and γ ($0 < \gamma \leq 1$) are the gain and the interference pattern visibility coefficients that are dependent on the beam-tail intensities at the PD locations. We assume that these coefficients are equal for all sensors. The static phase terms ϕ_l in (1) and ϕ_l' , ϕ_l'' , and ϕ_l''' in (2) are dependent on the l th PD's

coordinate at the sensing plane [27]. The measured signals $\{J_l(t)\}$, $l = 1, \dots, N_{\text{PD}}$, are sent to a feedback controller (an amplifier with controllable gain) that forms control voltages applied to the phase shifting elements, as shown in figure 1. The piston phases of the outgoing beamlets $\{\delta_j(t)\} = \{u_j(t) + \Delta_j\}$, $j = 1, \dots, N_{\text{sub}}$, are dependent on both the phase shifts $\{u_j(t)\}$ introduced by the fiber-integrated phase shifters and the relatively slow-varying (quasi-static on the scale of phase shifter response time) phase deviations (phase-noise terms) $\{\Delta_j\}$ in the multi-channel fiber system³.

The dynamics of the j th piston phase $u_j(t)$ in response to the applied control voltage U_j can be described by the first-order differential equation characterizing electrical charge of a capacitor associated with the j th fiber-integrated phase shifter,

$$\tau \frac{du_j(t)}{dt} + u_j(t) = gU_j [J_1(t), \dots, J_l(t), \dots, J_{N_{\text{PD}}}(t)], \quad (3)$$

where τ is the phase shifter response time and g is the electronic gain coefficient. In the most general case the terms $\{U_j\}$ in (3) are dependent on all sensor outputs $\{J_l\}$, and hence on all piston phases $\{\delta_j(t)\}$. The set of equations (3) can thus be represented in the following equivalent form:

$$\tau \frac{d\delta_j(t)}{dt} + \delta_j(t) = gU_j [\delta_1(t), \dots, \delta_j(t), \dots, \delta_{N_{\text{sub}}}(t)] + \Delta_j, \quad (4)$$

where $j = 1, \dots, N_{\text{sub}}$. We assume here that the phase-noise terms are slow-varying over the time τ , and for this reason their dependence on the time variable is neglected. The right-hand side of (4) can be ‘engineered’ by considering different combinations of sensor outputs. Here we distinguish two characteristic feedback control system architectures referred to as feedback control system with local and nonlocal spatial interactions. In the feedback system with local interactions, the dynamics of the transmitted beamlet piston phase $\delta_j(t)$ in equation (4) is solely defined by the sensors’ output signals that are dependent on $\delta_j(t)$. These sensors are located next to the j th subaperture. In contrast, in the system with nonlocal spatial interactions, the dynamics of the piston phase $\delta_j(t)$ is driven by the sensor outputs that are independent of $\delta_j(t)$. The notional schematics in figure 2 illustrate sensing and control system configurations with both local ((a), (c)) and nonlocal ((b), (d)) spatial interactions for systems with two-tail ((a), (b)) and three-tail ((c), (d)) sensing geometries.

3. Piston phase dynamics in fiber-array system with two-tail interference sensors

3.1. Local spatial interactions

Consider first a fiber-array system with local spatial interactions based on two-tail interference sensors as shown in figure 2(a). In this case, the control voltage U_j in

(4) is dependent only on the signal J_j given by (1). For fiber-integrated phase shifters, the dependence of the phase shift magnitude on the applied control voltage can be considered as a linear function within wide (up to $10\text{--}15\pi$ rad) phase modulation range [29]. Consequently, the dynamics of piston phases in this system can be described by the following set of independent nonlinear Debye-type equations:

$$\tau \frac{d\delta_j(t)}{dt} + \delta_j(t) = K \{1 + \gamma \cos [\delta_j(t) - \delta_0 + \phi_j]\} + \Delta_j, \quad (5)$$

where $j = 1, \dots, 6$ and $K \sim g\kappa$ is the gain coefficient. Note that a mathematical model similar to (5) has been used for analysis of nonlinear-feedback optical systems with local interactions, e.g., Kerr-slice/feedback-mirror system, nonlinear interferometers, and passive ring resonators [30–33]. In the set of equations (5), the piston phase of the central subaperture, $\delta_0(t)$, plays a role of a reference, with no control signal applied to the corresponding phase shifter. Therefore, at the time scale τ , $\delta_0(t)$ can be considered as a constant, i.e., $\delta_0(t) = \delta_0$. We assume that all phase shifts are defined with respect to the reference phase and hence in (5) δ_0 can be set to zero.

By setting temporal derivatives in equations (5) to zero, one can obtain the following equations for the steady-state solutions:

$$\hat{\delta}_j - \Delta_j = K \left[1 + \gamma \cos (\hat{\delta}_j + \phi_j) \right]. \quad (6)$$

The typical dependences of the steady-state solution $\hat{\delta}_j$ on the parameter K are shown in figures 3(a) and (b) for $\phi_j = 0$ and $\Delta_j = 0$, where stable steady-state solutions of (5) are shown by solid lines and unstable steady states by dashed lines. The unstable steady states separate attraction basins for trajectories of equations (5). For a fixed K , a piston phase trajectory $\delta_j(t)$ that starts at the initial point $\delta_j(t = 0)$ belonging to an attraction basin converges to one of $N_{\text{ss}}(K)$ stable steady-state solutions $\hat{\delta}^{(n)}(K)$, $n = 1, \dots, N_{\text{ss}}(K)$, as illustrated in figure 3. Thus, for a given value of gain coefficient K , several different stable steady states can be obtained by varying initial conditions. In nonlinear optics, such dynamics is commonly associated with optical multistability [34, 35].

In the numerical analysis performed for $\gamma = 1.0$, equations (5) were integrated over the time interval $T = 10\tau$ with different phase-noise terms $\{\Delta_j\}$ and initial conditions $\{\delta_j(0)\}$ using the fourth-order Runge–Kutta method [36]. The numerical simulations show that with the increase of K the average modulo 2π differences between the stationary piston phases of periphery subapertures approach to zero resulting in suppression of random phase shifts $\{\Delta_j\}$ for these subapertures. Note that this dynamics of piston phases occurs independently of both the MOPA-system-induced random phase shifts $\{\Delta_j\}$ and randomly chosen initial conditions $\{\delta_j(0)\}$. For a fixed K , the phase-noise suppression efficiency was characterized by the ensemble-averaged mean residual phase error $\bar{\varepsilon}_p(K) = 1/6 \sum_{j=1}^6 \langle \varepsilon_j^p(K) \rangle$. Here $\varepsilon_j^p(K) = \text{mod}_{2\pi} [\delta_j(T) - \bar{\delta}(T)]$ is the modulo 2π phase difference between the j th periphery subaperture and the mean value

³ The common source of the phase noise in the fiber system is related to phase shifts caused by variations in fiber lengths resulting from temperature fluctuations and mechanical deformations (acoustic waves and/or jitter). Frequency bandwidth of the phase noise is of the order of $10^2\text{--}10^3$ Hz.

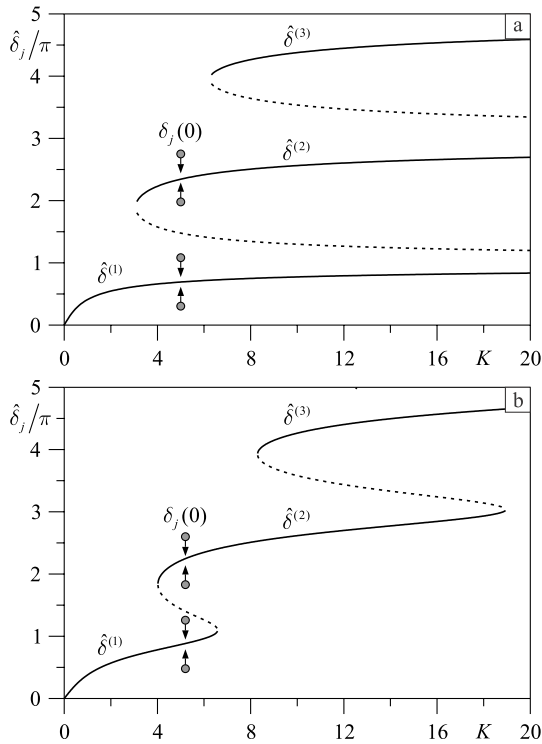


Figure 3. Steady-state solutions of equations (5) for the j th piston phase $\delta_j(t)$ versus gain coefficient K for $\phi_j = 0$, $\Delta_j = 0$, and $\gamma = 1.0$ (a) and $\gamma = 0.5$ (b). Solid and dashed lines correspond to stable and unstable solutions. Piston phase trajectories $\delta_j(t)$ starting at different initial conditions $\delta_j(0)$ indicated by gray circles are shown by arrows.

$\bar{\delta}(T) = 1/6 \sum_{j=1}^6 \delta_j(T)$. The averaging was performed using an ensemble of 500 random realizations of $\{\Delta_j\}$ and $\{\delta_j(0)\}$ with uniform probability distribution within $-\pi$ and π .

Contrary to the phase error for the periphery subapertures, the averaged mean residual phase error $\bar{\varepsilon}_{cp}(K) = 1/6 \sum_{j=1}^6 \langle \varepsilon_j^{cp}(K) \rangle$ characterizing the phase differences between the periphery and the central subapertures at $T \rightarrow \infty$ approaches a non-zero value $\bar{\varepsilon}_{cp}(K) = \hat{\delta}^{(1)}(K)$. Here $\varepsilon_j^{cp}(K) = \text{mod}_{2\pi}[\delta_j(T) - \delta_0]$ and $\hat{\delta}^{(1)}(K)$ is the stationary solution of equations (5) corresponding to the first (lowest) branch of the steady-state curve in figure 3. The residual phase errors $\bar{\varepsilon}_p(K)$ and $\bar{\varepsilon}_{cp}(K)$ obtained in numerical simulations are shown by small circles in figure 4(a).

Efficiency of the phase-noise suppression can be also characterized by the ensemble-averaged Strehl ratio $\langle St(K) \rangle = \langle I(\mathbf{r} = 0, K) \rangle / I_{dif}(\mathbf{r} = 0)$ defined as the ratio of the ensemble-averaged on-axis far-field intensity $\langle I(\mathbf{r} = 0, K) \rangle$ achieved in the fiber array with the feedback control and the diffraction-limited intensity $I_{dif}(\mathbf{r} = 0)$ corresponding to the perfectly phased fiber array with $\{\delta_j\} = \text{const.}$ for all subapertures. For the sensing and control system configuration corresponding to $\{\phi_j\} = 0$, the dependence $\langle St(K) \rangle$ is presented by small circles in figure 4(b). Due to the above-described uncompensated phase difference between the periphery and central subapertures, the achieved averaged Strehl ratio is relatively low ($\langle St \rangle \simeq 0.5$). Phase-noise compensation efficiency can be improved by controlling the

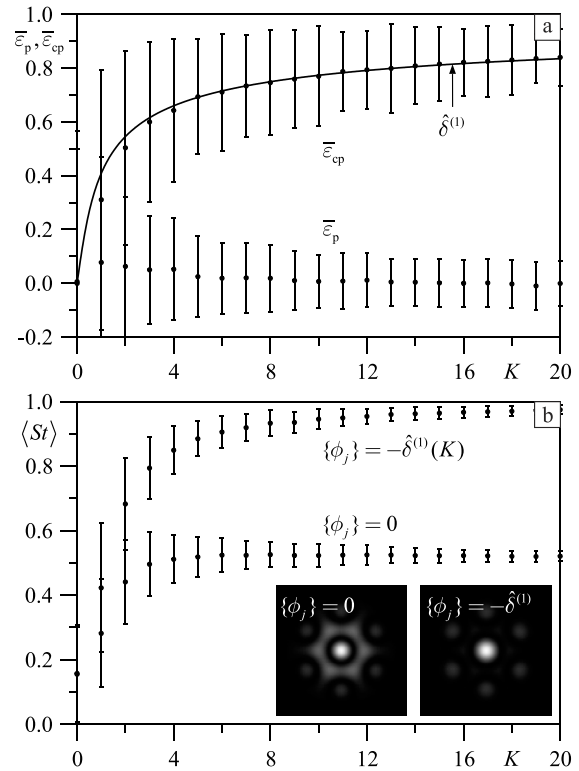


Figure 4. Efficiency of phase-noise suppression in the fiber-array system with local spatial interactions (see figure 2(a)), characterized by the ensemble-averaged residual phase errors $\bar{\varepsilon}_p(K)$ and $\bar{\varepsilon}_{cp}(K)$ in (a) and Strehl ratio $\langle St(K) \rangle$ in (b). The results are obtained by numerical integration of equations (5) over $T = 10\tau$ performed for $\gamma = 1.0$ and random realizations of phase-noise terms $\{\Delta_j\}$ and initial conditions $\{\delta_j(0)\}$. The Strehl ratio values in (b) are obtained for $\{\phi_j\} = 0$ and $\{\phi_j\} = -\hat{\delta}^{(1)}(K)$. The averaged values $\bar{\varepsilon}_p(K)$, $\bar{\varepsilon}_{cp}(K)$, and $\langle St(K) \rangle$ are presented by small circles while the corresponding standard deviations are shown by vertical bars. Solid line in (a) corresponds to the steady-state solution $\hat{\delta}^{(1)}(K)$ (see figure 3(a)). Grayscale images in (b) represent ensemble-averaged far-field intensity distributions of the combined beams with output phases $\{\delta_j(T = 10\tau)\}$ obtained for $K = 20$. The fiber-array parameters used in computations are described in [1, 25].

static phase shifts $\{\phi_j\}$. This can be achieved by lateral displacement of photo-detectors at the sensing module. Since the mean residual phase error $\bar{\varepsilon}_{cp}(K)$ in figure 4(a) approaches $\bar{\varepsilon}_{cp}(K) = \hat{\delta}^{(1)}(K)$, one can consider the photo-detectors' displacements that can compensate for these phase errors by introducing static phase shifts $\{\phi_j\} = -\hat{\delta}^{(1)}(K)$. The Strehl ratio data computed for this case are also presented in figure 4(b). As seen, for $K \geq 15$, one can obtain nearly ideal compensation of the MOPA-system-induced phase noise with $\langle St \rangle > 0.95$. This corresponds to locking of the outgoing beamlet phases at the fiber-array exit pupil. Contrary to the pupil-plane phase-locking techniques based on the gradient descent optimization [27], fiber-array phasing is achieved here by utilizing the described feedback control system with local spatial interactions. Phase-locking efficiency can also be evaluated by comparing the grayscale images shown in figure 4(b) of far-field intensity distribution of the combined beam for the fiber-array system of figure 2(a).

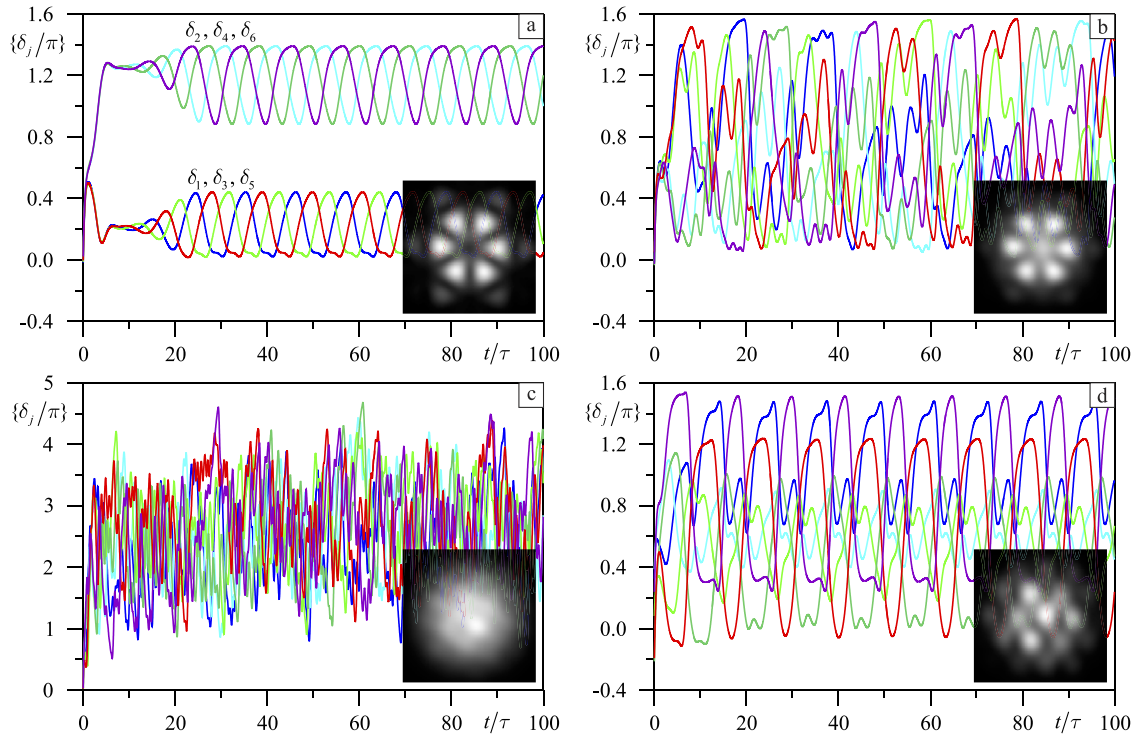


Figure 5. Temporal dynamics of piston phases $\{\delta_j(t)\}$ in the fiber array with nonlocal spatial interactions corresponding to the sensing and control system geometry in figure 2(b). The results are obtained by numerical integration of equations (7) with random initial conditions, $\gamma = 1.0$, $\{\phi_j\} = 0$, and different values of gain coefficient K : (a), (d) $K = 2.2$, (b) $K = 2.5$, and (c) $K = 8$. The phase-noise terms $\{\Delta_j\} = 0$ in (a)–(c) and are random with uniform probability distribution inside $[-\pi, \pi]$ in (d). Grayscale insets represent far-field intensity distributions of the combined beams averaged over 100τ . The fiber-array parameters are the same as in figure 4.

The far-field intensity obtained in the system with $\{\phi_j\} = -\hat{\delta}^{(1)}(K)$ practically coincides with the diffraction-limited pattern formed by the ideally phased fiber array.

3.2. Nonlocal spatial interactions

Consider now the fiber-array system with nonlocal spatial interactions defined by the sensing and control system geometry shown in figure 2(b). In this system, the dynamics of the j th piston phase is governed by the $(j + 1)$ th sensor output. Correspondingly, as follows from (1) and (4), the nonlinear dynamics of piston phases is described by the following set of differential equations:

$$\tau \frac{d\delta_j(t)}{dt} + \delta_j(t) = K \{1 + \gamma \cos[\delta_{j'+1}(t) - \delta_0]\} + \Delta_j, \quad (7)$$

where $j' = j$ for $j = 1, \dots, 5$ and $j' = 0$ for $j = 6$ (cyclic permutation). Note that similar type equations describe dynamic processes in nonlinear ring cavities with delayed feedback [37–39] and in a chain of coupled nonlinear interferometers with field rotation [10].

Consider the results of numerical integration of equations (7). With the gradual increase of the gain K , the dynamics of piston phases undergoes transition from the monostatic steady-state solution for $0 \leq K \leq 1.0$ to bistability with $\hat{\delta}_1 = \hat{\delta}_3 = \hat{\delta}_5$ and $\hat{\delta}_2 = \hat{\delta}_4 = \hat{\delta}_6$ for $1.0 < K \leq 2.0$. Further K increase leads first to the appearance of periodic and quasi-periodic oscillations, as illustrated in figures 5(a) and (b) for $K = 2.2$ and $K = 2.5$, respectively. The piston phase

oscillations at the fiber-array pupil-plane result in the far-field intensity distributions that display spatial periodicity even after averaging over several hundred of oscillation cycles. These time-averaged (long-exposure) far-field images are shown by grayscale insets in figures 5(a) and (b). For larger K , the periodic and quasi-periodic oscillations are transitioned to statistically independent chaotic oscillations of piston phases, as illustrated in figure 5(c) for $K = 8.0$. This results in an incoherent combination of transmitted beamlets with the nearly spatially homogeneous time-averaged far-field intensity pattern shown at the bottom of figure 5(c). The presence of phase noise described by the random terms $\{\Delta_j\}$ in equation (7) further complicates the dynamics. In the presence of noise, the boundaries of different nonlinear dynamical regimes are shifted, i.e., transitions between periodic, quasi-periodic, and chaotic oscillations appear at smaller or larger values of the gain coefficient K , as illustrated in figure 5(d) for $K = 2.2$. For large enough gain coefficients, however, the stochastic dynamics of systems with and without phase noise are practically indistinguishable.

Note that the incoherent combination of the transmitted beams in figure 5(c) is achievable over the time interval on the order of hundreds of τ . With the nanosecond-range time response of the fiber-integrated phase shifters, the time averaging is performed under the condition that the most common phase distorting factors including fiber-array-system-induced phase noise and/or refractive index inhomogeneities of laser beam propagation medium (e.g., atmosphere) are considered ‘frozen’ (static). This provides opportunities for the

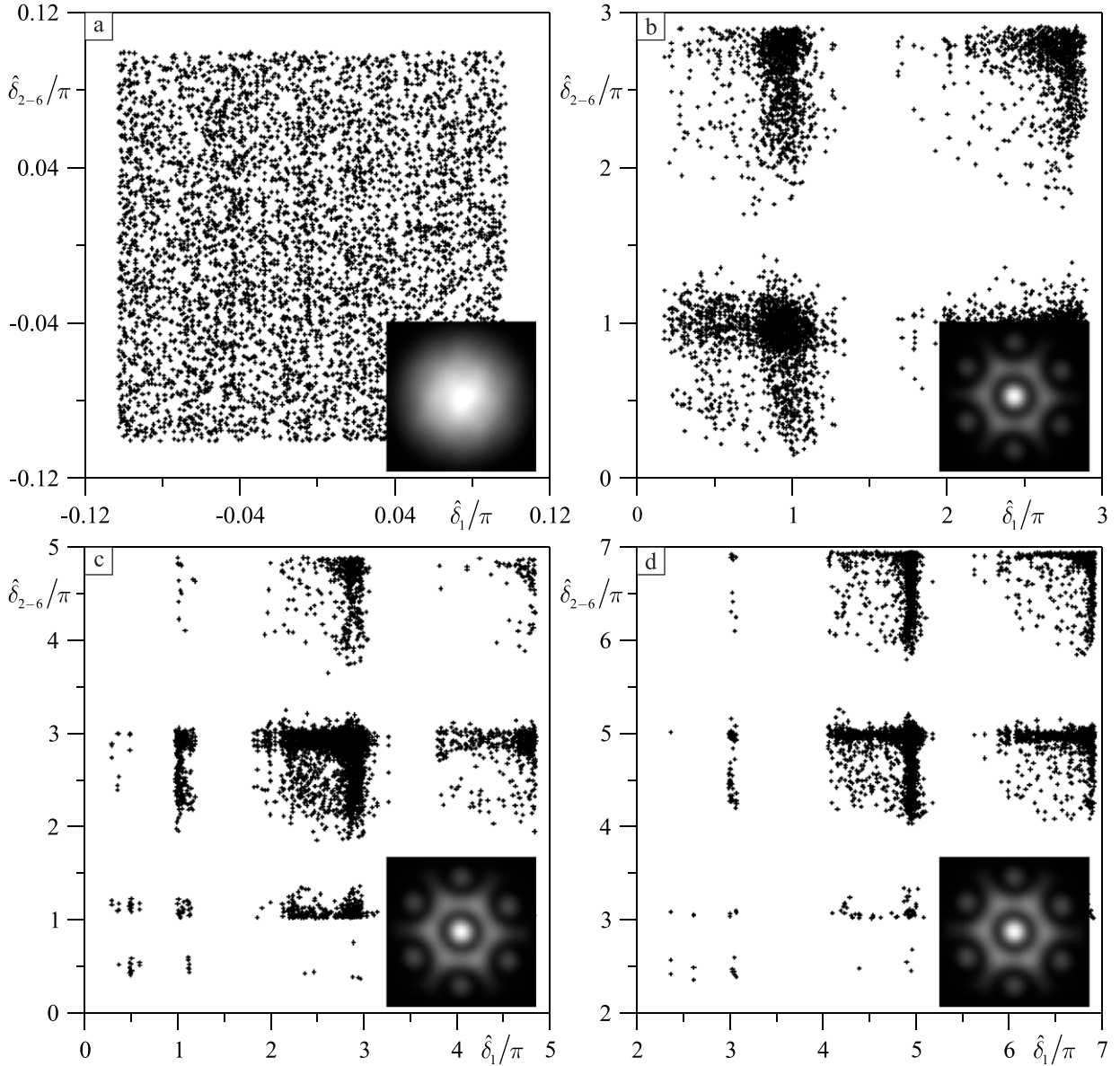


Figure 6. Scatter plots illustrating stationary solutions of equations (8), $\{\hat{\delta}_j\}, j = 1, \dots, 6$, for the feedback control system with three-tail interference sensors and local interactions for different values of gain coefficient K under the impact of piston phase noise $\{\Delta_j\}$: (a) $K = 0$, (b) $K = 4$, (c) $K = 8$, and (d) $K = 16$. Grayscale insets represent far-field intensity distributions of the combined beams computed by averaging 1000 instantaneous far-field intensities obtained for fiber array with piston phases in the corresponding scatter plots. The fiber-array parameters are the same as in figure 4.

generation of laser beams that can be considered as incoherent or partially coherent over the integration time of detectors commonly used in practical atmospheric optics applications such as free-space laser communications, directed energy, remote sensing, etc [40, 41].

4. Piston phase dynamics in fiber-array system with three-tail interference sensors

4.1. Local spatial interactions

Consider the fiber-array system with local spatial interactions that are realized using three-tail interference sensors in the arrangement shown in figure 2(c). The piston phase dynamics in this system can be described by the set of six coupled

equations,

$$\tau \frac{d\delta_j(t)}{dt} + \delta_j(t) = K_{j-1}J_{j-1}[\delta_0(t), \delta_{j-1}(t), \delta_j(t)] + K_j J_j[\delta_0(t), \delta_j(t), \delta_{j+1}(t)] + \Delta_j, \quad (8)$$

where J_j is the output signal (2) of the three-tail interference sensor neighboring to the $(j - 1)$ th and j th subapertures, and K_{j-1} and K_j are the gain coefficients that are assumed to be equal for all j . Note that here we omit the static phase terms dependent on the PDs' positions at the sensing plane. The subscript indices in (8) are obtained using cyclic permutations as shown in figure 2(c).

Since the nonlinear equations (8) are strongly coupled, analysis of the dynamics can be only performed through direct numerical simulations. In the numerical analysis, equations

(8) were integrated over the time interval $0 \leq t \leq T = 100\tau$ in a set of 1000 trials corresponding to statistically independent random phase-noise terms $\{\Delta_j\}$ and random initial conditions $\{\delta_j(t=0)\}$. In each trial the random values $\{\Delta_j\}$ and $\{\delta_j(t=0)\}$ were generated using a standard random number generator with uniform probability distribution inside the $[-\pi, \pi]$ interval. In all examined trials, the piston phase trajectories $\{\delta_j(t)\}$ resulting from numerical integration converge to one or another stationary solution $\{\delta_j(T=100\tau)\} \simeq \{\delta_j(T \rightarrow \infty)\} = \{\hat{\delta}_j\}$. Note that in the absence of the feedback control ($K = 0$) the piston phases of the outgoing beamlets converge to the random piston phases $\{\hat{\delta}_j\} = \{\Delta_j\}$ that are generated in the MOPA system. The control system dynamics described by equations (8) result in nonlinear transformation (mapping) of the initially random piston phases $\{\delta_j(t=0)\} = \{\Delta_j\}$ into a set of large number of stationary state phases $\{\hat{\delta}_j\} \neq \{\Delta_j\}$. This nonlinear mapping of random phases performed by the feedback control system is illustrated in figure 6 by two-dimensional scatter plots that characterize the relationship between values of stationary state piston phase of a single beamlet, $\hat{\delta}_1$, and the corresponding stationary state piston phases of all other beamlets, $\{\hat{\delta}_j\}, j = 2, \dots, 6$. Note that the piston phase of the central beamlet is used as a reference, i.e., we assume $\delta_0 = 0$. The scatter plot in figure 6(a) for the system without the feedback control corresponds to random piston phases $\{\hat{\delta}_j\} = \{\Delta_j\}$ (phase noise) with uniform probability distribution inside a square region $[-\pi, \pi]$. In the system with feedback control, this phase noise is transformed into highly non-uniform stationary piston phase distribution shown by the scatter plot in figure 6(b) for $K = 4$. This scatter plot is obtained in a set of 1000 trials of numerical integration of equations (8) for $\gamma = 1$ with random phases $\{\Delta_j\}$. As a result of nonlinear interactions, the piston phases of the outgoing beamlets group more densely along the horizontal and vertical line segments of length π that form the upper right corner of grid cells of size $2\pi \times 2\pi$. This means that the feedback system dynamics results in self-organization of piston phases leading to a drastic decrease of the MOPA-induced phase fluctuations at the fiber-array exit pupil. The phases of the output beamlets are not perfectly locked (phased), but with the increase of the feedback control gain (parameter K) their states become more and more localized (squeezed) (see figures 6(c) and (d) for $K = 8$ and 16). This results in the formation of a regular structure in the long-exposure far-field intensity distribution as shown by grayscale images in figure 6.

4.2. Nonlocal spatial interactions

Consider now as an example the three-tail fiber-array system with nonlocal spatial interactions as in figure 2(d). The corresponding equations for piston phases $\{\delta_j(t)\}, j = 1, \dots, 6$, can be represented in the form

$$\tau \frac{d\delta_j(t)}{dt} + \delta_j(t) = KJ_{j+1}[\delta_0(t), \delta_{j+1}(t), \delta_{j+2}(t)] + \Delta_j, \quad (9)$$

where J_j is the output signal of the three-tail interference sensor defined by the expression (2). The indices $(j+1)$ and $(j+2)$ in (9) are obtained using cyclic permutations.

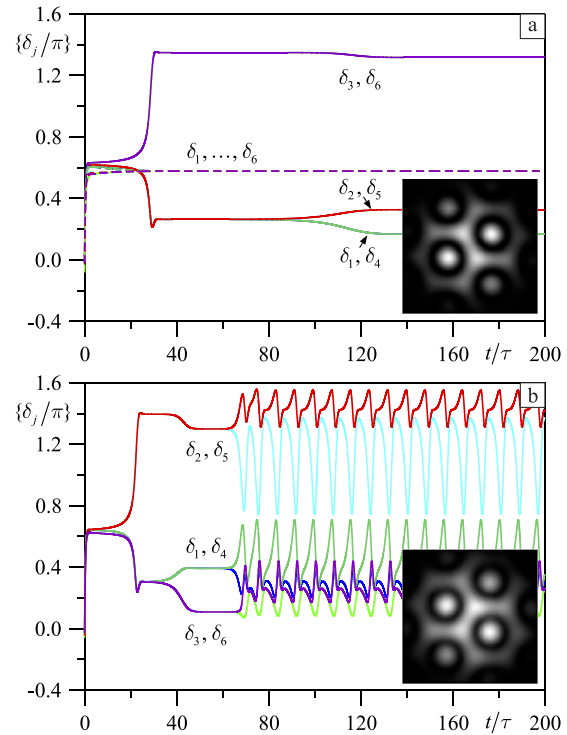


Figure 7. Temporal dynamics of piston phases $\{\delta_j(t)\}, j = 1, \dots, 6$, for the feedback control system with three-tail interference sensors and nonlocal spatial interactions for different values of gain coefficient K : (a) $K = 0.9$ (dashed lines) and $K = 1.1$ (solid lines), and (b) $K = 1.2$. In all cases, $\gamma = 1.0$ and $\{\Delta_j\} = 0$. Grayscale insets represent (a) instantaneous ($t = 200\tau, K = 1.1$) and (b) averaged over 100τ ($100\tau < t \leq 200\tau, K = 1.2$) far-field intensity distributions of the combined beams. The fiber-array parameters are the same as in figure 4.

Consider results of numerical analysis of the set of equations (9) in the absence of phase noise performed for $\gamma = 1.0$ and different values of the gain coefficient K . With gradual increase of K from zero to $K \simeq 1.0$, the piston phase trajectories $\{\delta_j(t)\}$ converge to a single steady-state solution $\{\delta_j(t \rightarrow \infty)\} = \hat{\delta}(K)$. The transition of piston phases to the steady-state solution for $K = 0.9$ is shown in figure 7(a) by dashed lines. With the gain coefficient increase over unity, the monostatic steady-state solution becomes unstable resulting in transitioning of piston phase trajectories to different steady-state solutions, as illustrated in figure 7(a) for $K = 1.1$. With further K increase, the multistatic solutions become unstable leading first to the development of periodic and quasi-periodic oscillations, as shown in figure 7(b) for $K = 1.2$, and then to uncorrelated chaotic oscillations.

5. Concluding remarks

We have shown that coherent fiber-array systems with feedback control of the outgoing beam piston phases based on a network of beam-tail interference sensors offer opportunities for engineering of a great variety of unconventional (exotic) laser beams with complex nonlinear spatio-temporal dynamics. Using as an example a fiber-array system with seven subapertures, we demonstrate that basic

ideas of self-organization in nonlinear optics can be directly applied to the coherent fiber-array systems, resulting in the generation of regimes similar to the nonlinear optics dynamical regimes, including spatial and temporal instability, patterns, spatio-temporal oscillations, and chaotic regimes. With the increase of the number of fiber-array subapertures and beam-tail interference sensors and the engineering of more complicated network of connections between sensors and phase shifting elements one can expect the generation of an even greater variety of different nonlinear dynamical regimes and unconventional laser beams that can be used for a number of applications including active imaging, directed energy, and laser communications.

Acknowledgments

This work was supported in part by the US Air Force Office of Scientific Research MURI Contract FA9550-12-1-0449 and by the US Navy SBIR Contract N68936-12-C-0136.

References

- [1] Vorontsov M A, Weyrauch T, Beresnev L A, Carhart G W, Liu L and Aschenbach K 2009 *IEEE J. Sel. Top. Quantum Electron.* **15** 269–80
- [2] Brignon A (ed) 2013 *Coherent Laser Beam Combining* (Weinheim: Wiley-VCH)
- [3] Vorontsov M A, Dumarevskii Y D, Pruidze D V and Shmal'gauzen V I 1988 *Izv. Akad. Nauk SSSR Ser. Fiz.* **52** 374–6
- [4] Abraham N B and Firth W J (ed) 1990 Special issue on transverse effects in nonlinear optics *J. Opt. Soc. Am. B* **7** 948–1373
- [5] Lugiato L A and El Naschie M S (ed) 1994 Special issue on nonlinear optical structures, patterns, and chaos *Chaos Solitons Fractals* **4** 1251–844
- [6] Vorontsov M A and Miller W B (ed) 1995 *Self-Organization in Optical Systems and Applications in Information Technology* (Berlin: Springer)
- [7] de Valcarcel G J, Roldan E and Vilaseca R (ed) 1998 Special issue on patterns in nonlinear optical systems *Quantum Semiclass. Opt.* **10** 775–878
- [8] Arecchi F T, Boccaletti S and Ramazza P L 1999 *Phys. Rep.* **318** 1–83
- [9] Akhmanov S A, Vorontsov M A and Ivanov V Y 1988 *JETP Lett.* **47** 707–11
- [10] Akhmanov S A, Vorontsov M A and Ivanov V Y 1989 Generation of the structures in the optical systems with 2D feedback: to creation of nonlinear optical analogies of neural networks *New Physical Principles of Optical Information Processing* ed S A Akhmanov and M A Vorontsov (Moscow: Nauka) pp 263–325
- [11] Akhmanov S A, Vorontsov M A, Ivanov V Y, Larichev A V and Zheleznykh N I 1992 *J. Opt. Soc. Am. B* **9** 78–90
- [12] Vorontsov M A 1993 *Quantum Electron.* **23** 269–71
- [13] Degtiarev E V and Vorontsov M A 1995 Optical design kit of nonlinear spatial dynamics *Self-Organization in Optical Systems and Applications in Information Technology* ed M A Vorontsov and W B Miller (Berlin: Springer) pp 45–67
- [14] Neubecker R, Oppo G L, Thuring B and Tschudi T 1995 *Phys. Rev. A* **52** 791–808
- [15] Arecchi F T, Boccaletti S, Ducci S, Pampaloni E, Ramazza P L and Residori S 2000 *J. Nonlinear Opt. Phys. Mater.* **9** 183–204
- [16] Nagaya T, Yamamoto T, Asahara T, Nara S and Residori S 2008 *J. Opt. Soc. Am. B* **25** 74–82
- [17] Vorontsov M A, Carhart G W and Dou R 2000 *J. Opt. Soc. Am. B* **17** 266–74
- [18] Yu M and Vorontsov M A 2004 *Proc. SPIE* **5552** 64–72
- [19] Ricklin J C and Davidson F M 2002 *J. Opt. Soc. Am. A* **19** 1794–802
- [20] Korotkova O, Andrews L C and Phillips R L 2004 *Opt. Eng.* **43** 330–41
- [21] Voelz D and Xiao X 2009 *Proc. SPIE* **7200** 72000C
- [22] Lajunen H and Saastamoinen T 2011 *Opt. Lett.* **36** 4104–6
- [23] Cai Y 2011 *Proc. SPIE* **7924** 792402
- [24] Vorontsov M A, Dudorov V V, Zyryanova M O, Kolosov V V and Filimonov G A 2013 *Atmos. Oceanic Opt.* **26** 185–9
- [25] Vorontsov M A and Lachinova S L 2008 *J. Opt. Soc. Am. A* **25** 1949–59
- [26] www.optonicus.com
- [27] Vorontsov M A, Lachinova S L, Beresnev L A and Weyrauch T 2010 *J. Opt. Soc. Am. A* **27** A106–21
- [28] Beresnev L A, Vorontsov M A, Weyrauch T, Carhart G, Lachinova S L and Liu J 2011 *Proc. SPIE* **7914** 79142Z
- [29] www.eospace.com
- [30] Lugiato L A and Oldano C 1988 *Phys. Rev. A* **37** 3896–908
- [31] Giusfredi G, Valley J F, Pon R, Khitrova G and Gibbs H M 1988 *J. Opt. Soc. Am. B* **5** 1181–92
- [32] Firth W J 1990 *J. Mod. Opt.* **37** 151–3
- [33] Vorontsov M A, Zheleznykh N I and Ivanov V Y 1990 *Opt. Quantum Electron.* **22** 501–15
- [34] Ikeda K 1979 *Opt. Commun.* **30** 257–61
- [35] Gibbs H 1985 *Optical Bistability: Controlling Light with Light* (New York: Academic)
- [36] Press W H, Teukolsky S A, Vetterling W T and Flannery B P 2007 *Numerical Recipes: The Art of Scientific Computing* 3rd edn (Cambridge: Cambridge University Press)
- [37] Ikeda K, Daido H and Akimoto O 1980 *Phys. Rev. Lett.* **45** 709–12
- [38] Otsuka K and Ikeda K 1987 *Phys. Rev. Lett.* **59** 194–7
- [39] Le Berre M, Ressayre E, Tallet A and Gibbs H M 1986 *Phys. Rev. Lett.* **56** 274–7
- [40] Vorontsov M A, Kolosov V V and Polnau E 2009 *Appl. Opt.* **48** A13–29
- [41] Vorontsov M, Weyrauch T, Lachinova S, Gatz M and Carhart G 2012 *Opt. Lett.* **37** 2802–4